EDITOR'S CHOICE: TRANSPORT PHENOMENA AND FLUID MECHANICS

An experimentally validated heat and mass transfer model for wax deposition from flowing oil onto a cold surface

Luqman Hakim Ahmad Mahir [ID] | Jieun Lee | H. Scott Fogler | Ronald G. Larson

Department of Chemical Engineering, University of Michigan, Ann Arbor, Michigan, 48109

Correspondence
Ronald G. Larson, Department of Chemical Engineering, University of Michigan, MI, USA.
Email: rlarson@umich.edu

Abstract

A transport model is proposed for wax deposition onto a cold finger from flowing wax-containing oils. The model solves transient energy and mass balances simultaneously for a reversible first-order kinetic rate for precipitation of pseudo-single-component wax, and the effects of yield stress using a critical solid wax concentration to withstand flow-induced stress at the deposit-fluid interface. The model can predict the time evolution of the deposit thickness, and the spatial and temporal evolution of temperature and wax concentration as validated using cold finger experiments. It was found that for high wax content oils, deposit thickness growth is dominated by heat transfer. For low wax content oils that are unable to gel, the thickness growth is slow and accompanied by occasional sloughing. Regardless of the mechanism controlling the growth, mass transfer cannot be neglected as wax diffusion into the deposit continues to take place after the deposit has stopped growing.

KEYWORDS

heat transfer, mass transfer, mathematical modeling, moving boundary problem, wax deposition

1 | INTRODUCTION

Paraffin deposition during crude oil transportation is a well-known problem in the upstream oil and gas field with few reliable solutions. In recent decades, modeling of wax deposition has been used to assess severity of deposition and devise appropriate strategies to manage deposition issues. Transport-based models help to describe deposition for various operating conditions even when field data are lacking. To construct such a model, an understanding of the physics and chemistry in the deposition process is necessary.

Paraffins in crude oil are a complex mixture of both normal and non-normal alkanes, with paraffin carbon numbers ranging anywhere from C5 all the way to C100+. The exact composition depends strongly on the geographical origin of the crude. This complex composition also gives rise to complex physical properties, which presents a challenge when trying to capture the physics necessary to understand the deposition process.

Paraffins remain dissolved in the oil phase until its temperature drops below the wax appearance temperature (WAT) where upon they start precipitating. Such solid–liquid mixtures possess viscoelasticity, plasticity, and a yield stress. The yield stress increases with increasing density of solid crystal, eventually forming a solid deposit. Numerous observations show that the incipient layer of a deposit contains both solid wax and entrapped fluid phase constituents.[1]

Wax deposition has been studied at lab scale and two theories have been developed based on experimental evidence. One theory suggests that the growth of wax gel/deposit is dictated by the rate at which soluble wax molecules get transported to the gel-oil interface. This mechanism is characterized by a slow growth of the gel thickness in which the heat transfer becomes pseudo-steady-state, and as a result the gel-oil interface starts out below the WAT and then rises as the gel grows outward.[1-3] If the gel-oil interface temperature reaches the WAT, which can occur if the oil temperature in the bulk oil is above the WAT, the gel thickness stops growing. However, even if the gel front has stopped moving, molecular diffusion carrying wax molecules from the oil into the gel can continue to take place, leading to the enrichment of precipitated wax over time in the gel for as long as the molecular-diffusion driving force exists. Numerous observations of gel thickness and gel composition as a function of time have supported this mechanism.[1,4,5]
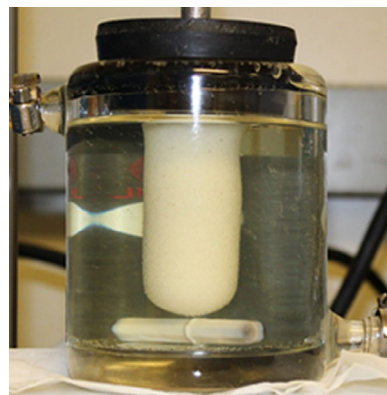
wileyonlinelibrary.com/journal/aic

The second theory suggests that the gel growth rate is explained by a transient heat transfer process.[6-14] This approach equates the migration of the gel-oil interface from a cold finger or from the inner surface of a pipe in a flow loop to the migration of the WAT isotherm (i.e., the gel-oil interface temperature is always at the WAT). This model thus assumes that fluid solidifies as soon as its temperature drops below the solubility temperature at which wax begins to precipitate, such that an arbitrarily small amount of precipitated crystal is sufficient to form a gel and to stop oil from flowing. This approach is able to describe the growth rate of a deposit formed from a binary n-alkane mixture[15] as well as a multicomponent wax mixture with a sharp bimodal normal distribution of wax carbon numbers[9] because the crystals that form are relatively large and that the solubility curve is steep for these systems. The composition of the deposit was also found to be nearly identical to the oil, at least very early in the deposition, when the gel is still growing.

Both mechanisms predict very distinct gel growth rates; thus a fair question would be: under what circumstances should one model be used over the other? In this work, we would like to address this question by (a) devising a model that includes transient heat transfer and transient mass transfer that are coupled, and (b) examining circumstances under which this comprehensive model reduces to the mass-transfer-controlled or heat-transfer-controlled mechanisms discussed above. This new model can help resolve the conditions under which neglect of various phenomena, such as mass-transfer limitations, pseudo-steady-state approximations, instantaneous crystallization kinetics, and effects of yield stress, might be justified. In the next section, we describe the materials and methods used in our experiments. We then describe our model and its mathematical derivation. Next, we introduce a characteristic length and a dimensionless group that serve as quick assessment of wax deposition characteristics. Finally, we compare the model predictions with experimental data.

2 | MATERIALS AND METHODS

2.1 | Deposition experiment

Deposition tests were carried out using a cold finger apparatus described in a previous publication.[15] In a typical setup, such as shown in Figure 1, a temperature-controlled glass-jacketed beaker containing waxy oil is continuously stirred with water flowing into the gap between the two glass walls at the bottom of the beaker and out at the top. The "cold finger" consists of a double-walled hollow 10-mm-outer-diameter cylindrical stainless steel tube with a circulating coolant flowing downward along the axis of the tube and then back upward in the annulus between the inner and outer walls of the tube. This cold finger, placed in the center of the container, maintains the temperature at value below the WAT. The outer surface of the stainless steel tube is colder than the stirred solution thereby causing a deposit to grow on it. Thermostated circulating water baths (not shown in Figure 1) control the temperatures of the cold finger and the water jacket.

FIGURE 1 A wax deposit forming on the cold finger. The lower right and upper left corners show the inflow and outflow ports for the jacket heating water [Color figure can be viewed at wileyonlinelibrary.com]

In a typical experiment, a waxy oil mixture is placed inside the jacketed beaker, where it is brought to a uniform controlled temperature by connecting the jacket to one of the circulating thermostatic baths. The cold finger is then inserted into the bulk oil to initiate deposition. A magnetic bar placed at the bottom of the jacketed beaker stirs the oil. The height of the oil in the jacketed beaker is 70 mm while the height of the cold finger that is immersed in the oil is 60 mm. The vortex that forms due to the stirring changes the height of the oil near the jacketed beaker as well as near the cold finger, thus affecting its immersion length, and the change in immersion depth is taken into account in the model. A binary mixture of oil and wax consisting of n-C12 and n-C28, respectively, was used in the tests.

The wax deposit thickness was obtained through the video recording of the deposition, which is made possible by the transparency of both the jacketed beaker and of the model oil used when the temperature is above the WAT. To determine how the n-C28 deposit composition changes with time, deposits formed at different times were collected from the cold finger by scraping off a 2-mm-thick layer at the outer edge of the deposit, and another 2-mm-thick layer from the inner edge next to the cold finger. When the deposit's total thickness was less than 4 mm, then the outer and inner scraping thicknesses were each half the total thickness of the deposit. After the acquisition of a deposit or oil sample in any run, the cold finger was cleared of all deposited wax, then the oil/wax mixture was replaced with a fresh mixture, and the deposition run was restarted from the deposit-free initial state.

High-temperature gas chromatography (HTGC) was used to measure the wax concentrations in these collected deposits. To maintain their uniformity, the samples were preheated using a heating plate prior to HTGC injection.

2.2 | Measurement of heat transfer coefficients

The model developed in Section 3 contains three heat transfer coefficients: U_{jac}, h_i and h_{cf} defined below. A set of experiments in the

absence of any deposition, that is, using the wax-free oil, were performed to obtain these coefficients. Temperature at various locations were measured in these experiments. Figure 2 shows the locations of thermocouples installed for this purpose.

U_{jac}, the overall heat transfer coefficient that characterizes the convective heat transfer rate from the heating water to the stirred oil in the jacketed beaker (without the cold finger), was measured by performing a transient heat transfer experiment. The jacketed beaker filled with a wax-free n-C12 was first equilibrated at 5°C under stirring by flowing cooling water through the jacket at 5°C. The cold jacketed beaker was then quickly connected to a heating water flow with T_{jac} at 35°C. The temperature of the stirred solution, T_b, increased due to the heating and eventually reached a new thermal equilibrium with $T_b = T_{jac}$. An overall energy balance around the oil, shown in Equation (1), was then used to fit U_{jac} to the measured time-dependent temperature.

$$\rho \hat{c}_p V_{oil} \frac{dT_b}{dt} = U_{jac} A_{jac} \left(T_{jac,avg} - T_b \right) \tag{1}$$

Here ρ denotes the oil density, $\hat{c}_p$ the oil specific heat capacity, V_{oil} the volume of oil in the jacketed beaker, A_{jac} the jacketed area, and $T_{jac,avg}$ the average between $T_{jac,in}$ and $T_{jac,out}$, where these two temperatures typically differed by around is 0.2°C.

Figure 3 shows how T_b obtained from Equation (1) compares to the actual T_b for different oil stirring rates.
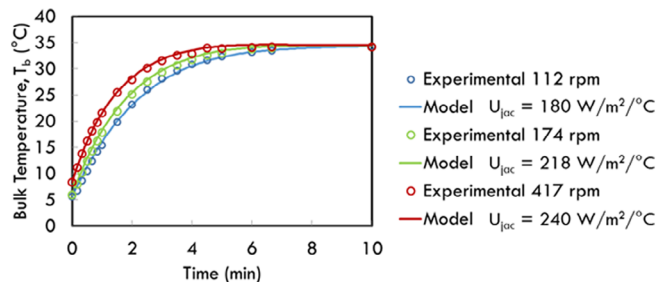
The coefficient h_i characterizes the convective heat transfer rate between the stirred oil and the surface of the cold finger while h_{cf} characterizes the convective heat transfer rate between the inner surface of the cold finger and the cooling water flowing inside the cold finger. Obtaining both coefficients requires first measuring U_i, the overall convective/conductive heat transfer coefficient for heat transported from the stirred oil to the cooling water. U_i was obtained by running the same transient heat transfer experiment as before, except with the cold finger simultaneously immersed in the oil. Equation (2) was used to fit U_i to the experimental data.

$$\rho \hat{c}_p V_{oil} \frac{dT_b}{dt} = U_{jac} A_{jac} \left(T_{jac,avg} - T_b \right) - U_i A_{cf,avg} \left(T_b - T_{cw,avg} \right) \tag{2}$$

Here $A_{cf,avg}$ is the average of the outer and inner surface areas of the cold finger that are immersed in the oil (where there is a 10% difference between the two; i.e., 19 vs. 17 cm^2) and $T_{cw,avg}$ is the average of $T_{cw,in}$ and $T_{cw,out}$, which typically differ by 0–1°C.

The coefficient h_i characterizes the convective heat transfer rate between the stirred oil and the surface of the cold finger, whereas h_{cf}

FIGURE 3 Bulk oil temperature, T_b versus time after supplying hot water to the jacket, used to determine the U_{jac} for different stirring rates [Color figure can be viewed at wileyonlinelibrary.com]
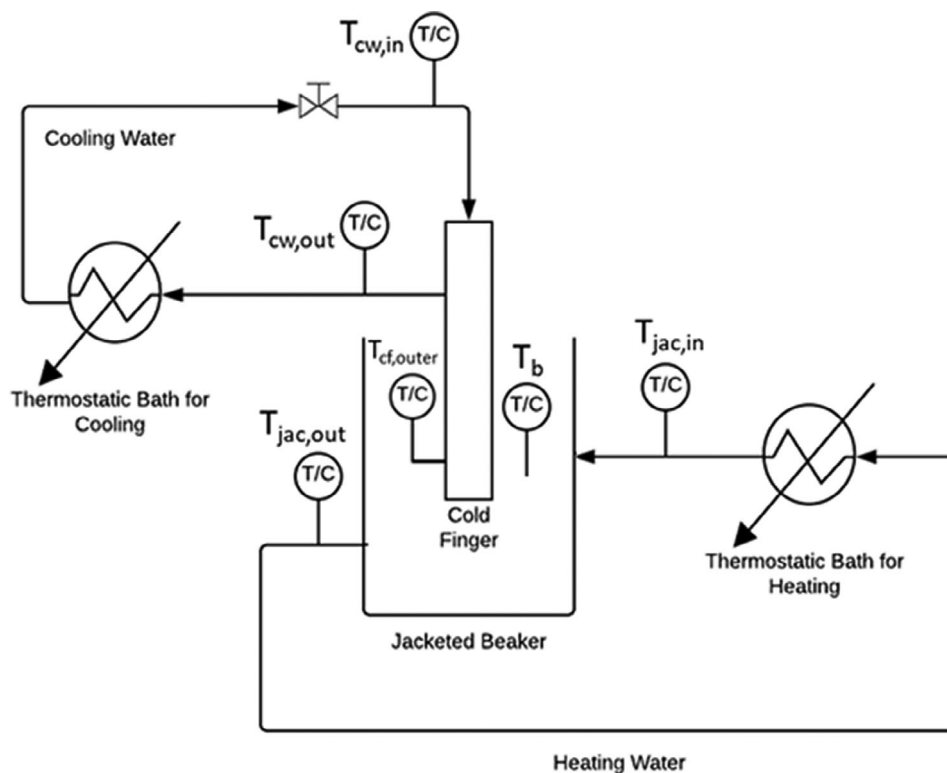
FIGURE 2 Schematic of the cold finger apparatus along with the location of six thermocouples. The thermocouple measuring $T_{cf,outer}$ is in contact with the outer surface of the cold finger

characterizes the convective heat transfer rate between the inner surface of the cold finger and the cooling water flowing inside the cold finger. Both h_i and h_{cf} can be derived from U_i. By the conservation of energy, assuming that the temperatures $T_{cw,avg}$ and $T_{cf,outer}$ adjust rapidly to any changes in T_b so that they are at pseudo-steady state, Equation (3) holds.

$$U_i A_{cf,avg}(T_b - T_{cw,avg}) = h_i A_{cf,outer}(T_b - T_{cf,outer}) \qquad (3)$$

Here $A_{cf,outer}$ is the outer surface area of the cold finger.

All of the temperature and surface area terms can be directly measured, and U_i was already obtained through the transient heat transfer test described previously, leaving h_i as the only unknown. Once h_i was determined, h_{cf} was calculated using the well-known analysis of series thermal resistances in series.

$$\frac{1}{U_i A_{cf,avg}} = \frac{1}{h_i A_{cf,out}} + \frac{r_{cf,out} \ln \frac{r_{cf,out}}{r_{cf,in}}}{k_{ss} A_{cf,out}} + \frac{1}{h_{cf} A_{cf,in}} \qquad (4)$$

where k_{ss}, $r_{cf,out}$, $r_{cf,in}$, and $A_{cf,in}$ denote stainless steel thermal conductivity, outer radius, inner radius, and inner surface area of the cold finger, respectively.

We assume that all heat transfer coefficients are unchanged from those for a wax layer depositing onto the cold finger, although we account for the time-dependent increase in $A_{cf,outer}$ due the growth of the deposit layer on the cold finger.

2.3 | Measurement of mass transfer coefficient

The mass transfer coefficient, k_c was determined by dissolving a pure wax slab into wax-free oil as shown in Figure 4. This process can be considered to be the reverse of deposition, in that soluble waxes migrate into the oil from the pure wax slab as opposed to the reverse of this during deposition.

Equations (5) and (6), which correspond to the heat and mass balances, respectively, evaluated at the slab-oil boundary, describe the time history of pure wax slab thickness δ during the dissolution.

$$\rho \Delta H \frac{d\delta}{dt} = h_i(T_b - T_i) - k \frac{dT}{dr_{i^-}} \qquad (5)$$

$$\rho \frac{d\delta}{dt} = k_c \left(C_{sb} - C_{s,eq,i}(T_i) \right) \qquad (6)$$

where ρ is the density of the pure wax slab, ΔH the specific latent heat of crystallization, h_i the heat transfer coefficient for the convective heat transfer rate at the slab-oil interface, T_i the interface temperature, $\frac{dT}{dr_{i^-}}$ the temperature gradient at the interface on the slab side, C_{sb} the concentration of soluble wax inside the oil, and $C_{s,eq,i}(T_i)$ the soluble wax concentration at its solubility limit at the interface. C_{sb} is zero at the beginning because the starting oil is wax-free, and $C_{s,eq,i}(T_i)$ is coupled to T_i through the solubility function.

Additionally, because thermal equilibrium is attained much more quickly than the time it takes for the slab dissolution to reach equilibrium, at pseudo-steady-state $\frac{dT}{dr_{i^-}} \sim \frac{(T_{cw,avg} - T_i)}{r_{cf,out} + \delta} \frac{1}{\ln\left(\frac{r_{cf,out}}{r_{cf,out} + \delta}\right)}$ is obtained from the steady heat conduction equation in radial coordinates. T_b, T_i, C_{sb}, and δ are all unknowns that evolve with time. The rest of the parameters are constants. To obtain T_b, T_i, C_{sb}, and most importantly δ, Equations (5) and (6), along with an energy balance of the oil and a mass balance of wax in the oil are simultaneously solved.

This technique works well because (a) there is no diffusion inside the pure wax slab, thus simplifying the model, and (b) the rate at
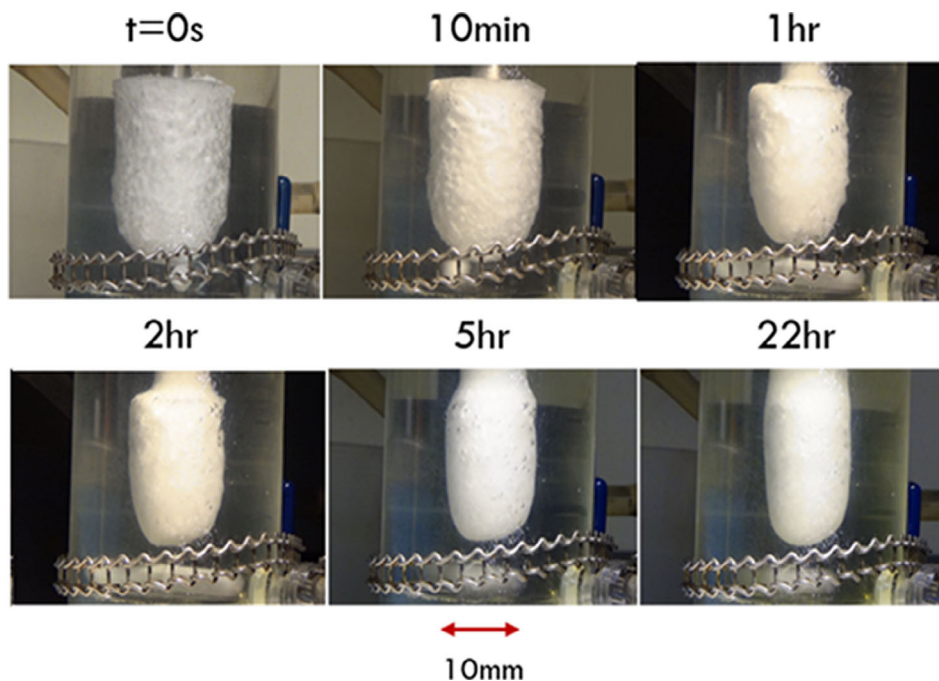
FIGURE 4 Dissolution of pure wax slab (n-C28) into an initially wax-free n-C12. The solid–liquid interface stops receding when the oil becomes fully saturated [Color figure can be viewed at wileyonlinelibrary.com]

which wax dissolves into the oil is always limited by the rate of mass transfer at the interface, allowing k_c to be determined. For this method to work, the rest of the parameters, including the heat transfer coefficients, must be measured or known a priori, allowing the single remaining parameter k_c to be obtained by matching the model prediction to the experimental dissolution profile.

Figure 5 shows how a single value of $k_c = 1 \times 10^{-5}$ m/s can describe the dissolution profile at different jacket temperatures at a given stirring rate. If the stirring rate is changed, a new k_c must be re-determined from a dissolution experiment at that stirring rate.

3 | WAX DEPOSITION MODEL

Our model assumes the existence of thin heat transfer and mass transfer boundary layers at the deposit-oil interface across which temperature and wax concentration vary from uniform values in the stirred oil to surface values at the leading edge of the deposit. Our measurements of temperature and wax concentration far from the inner and outer surfaces of the stirred oil are in agreement with this assumption. This behavior is expected due to mixing induced by the agitation of the magnetic stir bar.

The steep temperature and wax concentration profiles inside the boundary layer are not resolved in our model. Instead, we compute the overall energy and mass exchanged at this interface and assume there is no accumulation of energy nor mass within that layer.[16] As shown in Figure 6, a thin control volume that encases the boundary layer is taken to be moving with front of the deposit toward the right at a speed $\frac{d\delta}{dt}$, where δ is the deposit thickness and t is time. Any energy or mass that enters this control volume through the oil side (right) leaves the control volume through the deposit side (left), and vice versa. Next, the mass and energy balances across this thin volume will be derived.

Across this mass transfer boundary layer the dissolved, or soluble, wax concentration C_s changes from that in the bulk oil, C_{sb}, which is to the right of the control volume, to the dissolved wax concentration just behind (i.e., to the left of) the interface, C_{si}. The flux of wax is

given by the product of the difference of these concentrations, that is, the driving force, times the mass transfer coefficient k_c. On the left side there is a flux of dissolved wax diffusing further into the deposit according to Fick's Law. As the control volume moves into the oil domain, it sweeps in mass from the right, and leaves behind mass on its left side. As a result, there is a mass flux on the right side of the interface equal to $C_{sb}\frac{d\delta}{dt}$ while on the left hand side it is $\left(C_{pi} + C_{si}\right)\frac{d\delta}{dt}$, where C_{pi} is the solid (or precipitated) wax concentration C_p at the interface. If the oil temperature is below its WAT, there will also be precipitated waxes present in the oil with concentration C_{pb}. In this situation, an additional apparent flux, $C_{pb}\frac{d\delta}{dt}$ will appear on the right hand side of the moving boundary. In our experiments reported here, the oil temperature is always above WAT, so that C_{pb} is zero. The interfacial wax mass balance can be then summarized as follows:

$$D_{eff}\frac{\partial C_s}{\partial r} + \left(C_{pi} + C_{si}\right)\frac{d\delta}{dt} = k_c\left(C_{sb} - C_{si}\right) + \left(C_{sb} + C_{pb}\right)\frac{d\delta}{dt} \quad (7)$$

where D_{eff} is the effective diffusivity of soluble wax inside the gel/deposit near the interface.

A similar equation can be derived for the interfacial energy balance equation, using the same control volume moving at the same speed $\frac{d\delta}{dt}$ as the mass-transfer control volume. The temperatures on left and right side of the interface are shown in Figure 6b.

On the right side of the interface, there is a heat transfer boundary layer across which the temperature changes from the bulk oil temperature, T_b, to the surface temperature, T_i, the difference being the driving force. On the left side, the heat flux into the deposit is given by the Fourier's Law. Similar to the variation in wax concentration across the interface, there should also be a variation in sensible heat content from $\rho\hat{c}_p T_b$ to $\rho\hat{c}_p T_i$, assuming, as is reasonable, that ρ and $\hat{c}_p$ of the oil and of the deposit are very similar. Therefore, an additional term therefore appears on either side of the heat balance equation that takes into account this difference in sensible heat across the interface. Similar terms on either side account for the latent heat ΔH
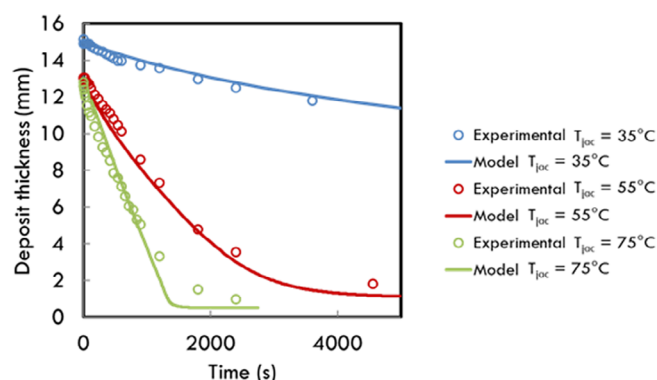
FIGURE 5 Dissolution profiles of n-C28 into n-C12 for different jacket temperatures at a stirring rate of 174 rpm. All of the curves were generated from the model using $k_c = 1 \times 10^{-5}$ m/s [Color figure can be viewed at wileyonlinelibrary.com]
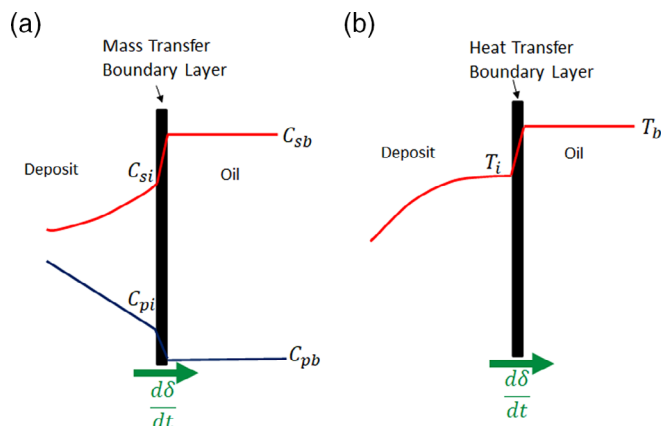
FIGURE 6 (a) The moving mass transfer boundary layer. (b) The moving heat transfer boundary layer [Color figure can be viewed at wileyonlinelibrary.com]

released during the formation of solid waxes. The interfacial energy balance can be summarized as follows:

$$k\frac{\partial T}{\partial r} + \rho\hat{c}_p T_i\frac{d\delta}{dt} - C_{pi}\Delta H\frac{d\delta}{dt} = h_i(T_b - T_i) + \rho\hat{c}_p T_b\frac{d\delta}{dt} - C_{pb}\Delta H\frac{d\delta}{dt} \quad (8)$$

where k is the gel/deposit thermal conductivity, and ΔH the specific latent heat of crystallization.

Next, the heat and mass balance equations to be solved in the deposit and oil domains are derived. Because of the uniformity of the deposit along the cold finger axis (see Figure 1), energy and mass transfers in the axial and tangential directions can be neglected. The energy balance in the deposit domain is given by the time-dependent, axisymmetric energy balance:

$$\rho\hat{c}_p\frac{\partial T}{\partial t} = k\frac{1}{r}\frac{\partial}{\partial r}\left(r\frac{\partial T}{\partial r}\right) + \Delta H\frac{\partial C_p}{\partial t} \quad (9)$$

On the right side of Equation (9), the first term represents heat conduction, while the second term represents latent heat release due to precipitation (or latent heat absorption in the case of a dissolution). The second term is present because further precipitation inside a deposit occurs during deposit aging.

The flux boundary conditions necessary to solve Equation (9) are:

$$\text{B.C.'s}\begin{cases} h_{cf}(T - T_{cw,avg}) = k\frac{\partial T}{\partial r} \text{ at } r = r_{cf,out} \\ k\frac{\partial T}{\partial r} + \rho\hat{c}_p T_i\frac{d\delta}{dt} = h_i(T_b - T) + \rho\hat{c}_p T_b\frac{d\delta}{dt} + (C_{pi} - C_{pb})\Delta H\frac{d\delta}{dt} \text{ at } r = r_{cf,out} + \delta \end{cases} \quad (10)$$

At the boundary between the cold finger's wall and the inner edge of the deposit ($r = r_{cf,out}$), the temperature drop across the stainless steel tube wall has been neglected in Equation (10). This omission is reasonable because the thermal conductivity of stainless steel is two orders of magnitude greater than the thermal conductivity of n-alkanes, and the stainless steel tube wall is quite thin ($\sim$1 mm), leading to negligible resistance to heat transfer through the wall. At the moving interface ($r = r_{cf,out} + \delta$), Equation (8) is used as the boundary condition.

In the stirred solution domain, we assume the temperature to be spatially uniform, which we validated experimentally. The transient energy balance is:

$$\hat{c}_p\frac{d}{dt}(m_{liq}T_b) = U_{jac}A_{jac}(T_{jac} - T_b) - h_i A_i(T_b - T) \quad (11)$$

where m_{liq} is the mass of stirred solution.

By simultaneously solving Equations (9) and (11), radial and temporal variations of temperature in the deposit are resolved, as well as the temporal variation in the stirred solution temperature.

For the mass balance equations, it is assumed that all constituents in the mixture can be lumped into one of three categories: dissolved waxes, precipitated waxes and solvent. The mass balance for the dissolved waxes in the deposit is derived in an analogous manner to the energy balance inside the deposit:

$$\frac{\partial C_s}{\partial t} = \frac{1}{r}\frac{\partial}{\partial r}\left(rD_{eff}\frac{\partial C_s}{\partial r}\right) - k_r(C_s - C_{s,eq}[T]) \quad (12)$$

where k_r is the precipitation/dissolution rate constant and $C_{s,eq}$ is the solubility limit of waxes at a given temperature.

The first term on the right hand side describes the diffusion of dissolved wax, while the second term describes the rate by which dissolved waxes precipitate. The precipitation process is modeled as a reversible first order reaction with driving force given by the difference between the local concentration and the solubility limit. Note that Equation (12) also accounts for dissolution in situations where the local concentration is below the solubility limit. The relevant boundary conditions are: (a) no penetration at the cold finger outer wall and (b): a flux boundary condition at the deposit-oil interface:

$$\text{B.C.'s}\begin{cases} D_{eff}\frac{\partial C_s}{\partial r} = 0 \text{ at } r = r_{cf,out} \\ D_{eff}\frac{\partial C_s}{\partial r} + (C_{si} + C_{pi})\frac{d\delta}{dt} = k_c(C_{sb} - C_{si}) + (C_{sb} + C_{pb})\frac{d\delta}{dt} \text{ at } r = r_{cf,out} + \delta \end{cases} \quad (13)$$

Similar to the temperature, the dissolved wax concentration in the stirred solution is also assumed to be uniform throughout the liquid mixture.

We also need to solve for the mass balance of precipitated waxes in the deposit. It is assumed that precipitated waxes are immobilized when they form in the deposit and do not diffuse. The precipitated waxes are assumed to be a continuum rather than as discrete particles, where their formation (and dissolution) can be described as follows:

$$\frac{\partial C_p}{\partial t} = k_r(C_s - C_{s,eq}[T]) \quad (14)$$

Unfortunately, solving Equation (14) can be numerically expensive because when k_r is relatively large, a very small time step size is required to ensure stability and convergence of the numerical solution. To avoid this problem, we instead compute the precipitated wax concentration C_p by solving the total wax mass balance, which is derived by simply adding Equation (14) to Equation (12):

$$\frac{\partial C_p}{\partial t} + \frac{\partial C_s}{\partial t} = \frac{1}{r}\frac{\partial}{\partial r}\left(rD_{eff}\frac{\partial C_s}{\partial r}\right) \quad (15)$$

The rate of wax deposition still appears in Equation (12) where it can influence the solution to the mass balance.

In the deposit, the precipitated waxes form an interlocking network of solid wax crystals, resulting in a more tortuous pathway for wax molecules in the liquid phase that are diffusing further into the deposit. This increased tortuosity leads to a decrease in the effective diffusivity of the molecules relative to that in a precipitate-free oil. In solid-free oils, the diffusivity of dissolved wax is captured well by the Hayduk-Minhas equation[17]:

$$D_{w/o} = 13.3\left(10^{-12}\right)(T+273.15)^{1.47}\mu^{\left(\frac{10.2}{V_A}-0.791\right)}V_A^{-0.71} \qquad (16)$$

where μ is the precipitate-free oil viscosity, and V_A is the molar volume of the wax molecule. For our n-C28/n-C12 model oil, we use Equation (17) to describe μ, which was obtained by fitting n-C12 experimental viscosities at different temperatures.

$$\mu = 1.6 \times 10^{-2}\exp\left(\frac{1334}{T+273.15}\right) \qquad (17)$$

In the deposit, we use an empirical correlation from Cussler[18] to describe the effective diffusivity of wax molecules, D_{eff}, which takes into account the local solid wax content:

$$D_{eff} = \frac{D_{w/o}}{1 + \frac{K_\alpha^2\left(\frac{C_p}{\rho}\right)^2}{1-\frac{C_p}{\rho}}} \qquad (18)$$

Here, K_α is a dimensionless parameter identified as the wax crystal aspect ratio, and C_p again is the mass concentration of precipitated wax, so that $\frac{C_p}{\rho}$ is the volume fraction of precipitated solid. D_{eff} varies both spatially and temporally not only because of temperature changes but also because $\frac{C_p}{\rho}$ increases with time during deposit aging, leading to a gradual decrease in D_{eff}. When no precipitated wax is present, D_{eff} is on the order of 10^{-10} m^2/s, but it can decrease by multiple orders of magnitude as $\frac{C_p}{\rho}$ rises.

In the stirred solution, a simple overall wax mass balance can be used to calculate the remaining wax in the stirred solution at any time, t:

$$m_{total\ wax} = \left(C_{sb}+C_{pb}\right)V_{liquid} + 2\pi L_{cf}\int_{r_{cf,outer}}^{r_{cf,outer}+\delta}(C_s+C_p)r\,dr \qquad (19)$$

where $m_{total\ wax}$ is the total mass of wax present in the system, that is, deposit + solution, V_{liquid} the volume of oil in the reservoir, and L_{cf} the length of the deposit along the cold finger axis. V_{liquid} also equals $\pi r_{jac}^2 L_l - \pi(r_{cf,outer}+\delta)^2 L_{cf}$, where r_{jac} and L_l are the jacketed beaker radius and height of the liquid in the beaker, respectively.

At this point we have derived all the energy and mass balances necessary for both domains. What remains is to derive the equations describing how the deposit-oil interface evolves with time in order to solve for its rate of growth $\frac{d\delta}{dt}$. At the interface, the solid wax concentration is taken to be at C_{pi} due to the assumption that C_{pi} is the solid wax concentration required to resist erosion under the flow-induced stress at the interface. In mathematical terms, this implies that the substantial derivative of C_p at the interface is zero at all times:

$$\frac{\partial C_p}{\partial t}\bigg|_{i^-} + \frac{d\delta}{dt}\frac{\partial C_p}{\partial r}\bigg|_{i^-} = 0 \qquad (20)$$

where the subscript i^- indicates that the derivatives are evaluated at the interface on the deposit side. Equation (20) can be rearranged to express the deposit growth rate $\frac{d\delta}{dt}$ in terms of the partial derivatives:

$$\frac{d\delta}{dt} = -\frac{\frac{\partial C_p}{\partial t}\big|_{i^-}}{\frac{\partial C_p}{\partial r}\big|_{i^-}} \qquad (21)$$

The finite difference method is used to solve the system of partial differential equations. The model uses the central difference scheme for space discretization and the backward Euler scheme for integrating with respect to time.[19,20] The deposit domain is discretized into 50 nodes. The oil domain is not discretized because of the uniformity in temperature and wax concentration (due to agitation). The algorithm used to solve the deposition model described is summarized in Figure B-1 in the Supplementary Information. We examined the model predictions under various limits to understand the behavior of the model. These analyses can be found in the Supplementary Information.

## 4 | COMPARISON BETWEEN THEORY AND EXPERIMENTS

Changing the stirring rate in the cold finger system is expected to have effects analogous to those produced by changing the flow rate in a pipe flow. Heat and mass transfer rates are expected to be larger due to enhanced convective transport (corresponding to higher heat and mass transfer coefficients). In addition, a higher flow rate and thus a higher wall shear stress should shift C_{pi} to a higher value as a deposit with a higher solid content is required to withstand the higher stress imposed. To determine if C_{pi} influences significantly the growth rate of wax deposits in the cold finger apparatus, experiments were carried out at different stirring rates.

In these tests, the jacketed beaker setting temperature, T_{jac}, was maintained at 35°C, and the cold finger thermostatic bath set point, T_{cf}, was kept constant at 5°C. Figure 7 shows the deposit thickness as a function of time for a binary mixture consisting of 90 wt% n-C12 and 10 wt% n-C28 at the three different stirring rates of 112, 174, and 417 rpm, where rates higher than these were avoided to prevent the vortex height from exceeding the height of the container. Because of the dependence of the vortex height on stirring speed, the height of the cold finger immersed in the oil and the surface area of the jacket beaker in contact with the oil changed with stirring speed, and these changes are accounted for in the modeling.

Figure 7 shows that the deposit thickness increases over a period of around 30 min and then reaches a plateau. As the deposit thickens, it increasingly insulates the cold finger from the heat of the oil bath, eventually decreasing the heat flow into the cold finger to the point that it can be balanced by the heat flow from the jacket to the reservoir, so that the heat-transfer Biot number $\frac{h_l\delta}{k}$ reaches approximately unity, leading to the steady state. When the stirring rate increases, we see in Figure 8 that the steady-state deposit thickness decreases. At the higher stirring rate, the measured heat transfer coefficient, given in Figure 9, is higher, and a thinner deposit thickness δ, with a steeper temperature gradient and faster heat diffusion, is able to balance the heat transfer from the bath and bring the Biot number $\frac{h_l\delta}{k}$ to near unity, producing a steady state.
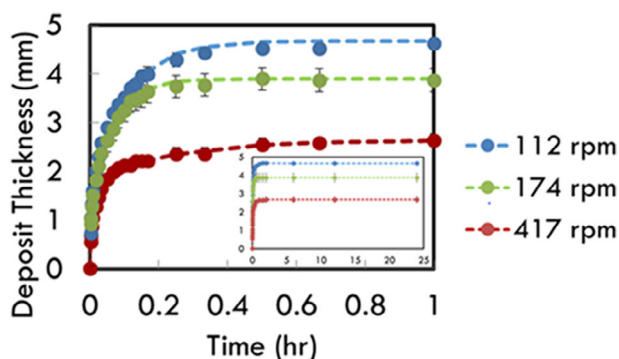
FIGURE 7 Deposit thickness versus time at different stirring rates, keeping T_{jac} at 35°C and T_{cf} at 5°C. Inset shows deposit thickness up to 25 hr. The dashed lines serve as a guide to the trend [Color figure can be viewed at wileyonlinelibrary.com]
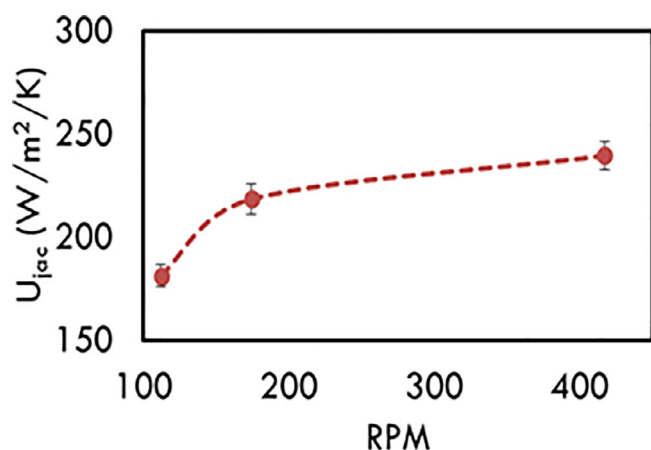
FIGURE 8 Overall jacket heat transfer coefficient, U_{jac} as a function of stirring rate [Color figure can be viewed at wileyonlinelibrary.com]
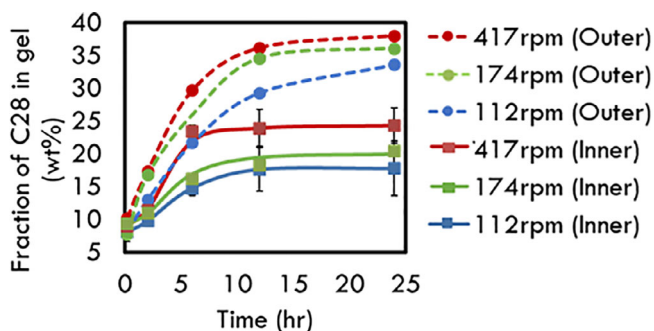
FIGURE 9 Fractions of C28 in the deposit from the outer and inner edges of the deposit as a function of time [Color figure can be viewed at wileyonlinelibrary.com]

It is important to remember that the critical solid wax concentration C_{pi} may also increase with increasing stirring rate. Thus, the decreasing deposit thickness with increasing stirring rate may not be completely explained by the increase in heat transfer coefficient alone, but could also be due to an increase in C_{pi}. However, as we will show, our experiments *with a single-component wax* have practically no influence of C_{pi}, which can therefore be taken to be zero.

Samples of the wax deposit were analyzed using HTGC after being collected from the outer edge of the deposit, which is directly behind the gel-oil interface, and from the inner edge, which is on the outer cold finger wall at the different times. Figure 9 shows that the fractions of the n-C28 in the outer and inner edges of the deposit, which includes both precipitated n-C28 and dissolved n-C28 trapped in the pore spaces of the deposit, start at the bulk solution value of 10 wt% and increase with time, even well after the deposit thickness plateaus at around 30 min (see Figure 7). These results indicate that n-C28 in the bulk oil continues to diffuse into the gel, densifying the precipitated wax deposit. Figure 9 also demonstrates that the fraction of n-C28 is higher with a higher stirring rate. This experimental observation is a consequence of the thinner deposit and hence the increase in the concentration-gradient driving force for diffusion. In addition, the mass transfer coefficient k_c also increases with the stirring rate (Figure 10), which delivers more wax to the deposit.

Note that, over time, the fraction of n-C28 at the outer edge of the deposit becomes higher than at the inner edge. Owing to the initially fast growth of the deposit which is the result of the gelation of the oil, its composition of n-C28 is initially nearly uniform at around that of the bulk oil; that is, around 10 wt%. The faster rate of wax enrichment at the outer edge compared to the inner edge can be reasoned by examining the change in wax solubility behavior as a function of radius. Wax solubility at the outer edge of the deposit is higher than that at the inner edge due to the temperature differences. The wax solubility for n-C28-nC12 binary mixture as a function of temperature has an exponential behavior.[15] The temperature profile across the deposit is close to being linear, thus the soluble wax concentration as a function of radius when at equilibrium is similar in shape to that of its wax solubility curve, that is, exponential. This would result in a steeper concentration gradient, causing a higher diffusion rate at the outer edge when compared to the inner edge. This eventually leads to the outer edge becoming enriched in solid at a faster rate than the inner edge. The diffusion coefficient is also higher at the outer edge due to the higher temperature, but this contribution is insignificant.

We now use the model to simulate the results of deposition at the lowest and highest stirring rates, 112 and 417 rpm. All parameters are listed in Table F-1 in the Supplementary Information. We take the precipitation rate constant k_r to be 1 s^{-1}, which is asymptotically fast so that higher values produce the same results, and C_{pi} is taken to be 0.
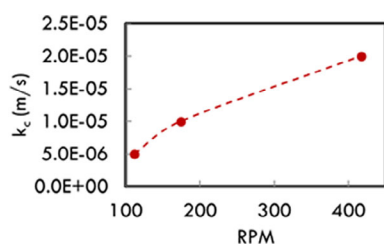
Figures 11 and 12 show that for the lowest stirring speed the model captures nearly quantitatively the deposit thickness growth as well as the time evolution of deposit composition by assuming fast precipitation and $C_{pi} = 0$, which implies that the wax forms a gel as soon as the first precipitates form.

The corresponding good agreement between predictions and measurements for the fastest stirring speed, 417 rpm, are shown in Figures 13 and 14, again with the same values of k_r and C_{pi}, but with

increased values of heat and mass transfer coefficients, in accord with the values given in Table F-1 in the Supplementary Information. Comparing these results with those of Figures 11 and 12 shows that the deposit thickness decreases with increasing stirring rate. Since the same model predicts both results for high and low stirring speeds, with the same model and model parameters except for the measured heat and mass transfer coefficients and to some extent the height of the liquid and the cooling water temperature, it follows that the thinner deposit at higher stirring speed can be explained solely by the increase in heat and mass transfer rates in the jacketed beaker.
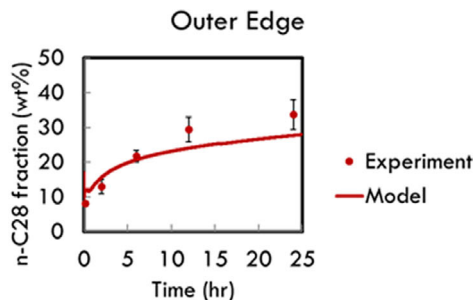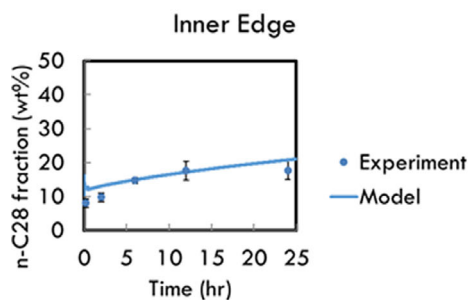
These comparisons show that: (a) the model successfully captures deposition in the cold finger at two stirring rates, and (b) the binary n-C12-n-C28 model oil does not behave like a complex wax mixture due to the fact that it easily forms a solid gel at low C_{pi}, low enough

to be set to zero, and the deposit growth rate is predominantly controlled by the heat transfer rate.

A condition that could push deposit growth into the mass-transfer-controlled regime is when C_{pi} is significantly above zero. To demonstrate such a case, we ran a deposition experiment using a dilute waxy model oil composed of 0.8 wt% n-C36 in a mineral oil that was barely able to form a gel at a temperature as low as 5°C due to its low wax content despite having a WAT of 40°C. We found that the growth of gel thickness of this oil at 5°C cold-finger temperature was not only slow and unable to be explained by transient heat transfer, but was also non-monotonic, with the gel sometimes breaking free from the cold finger and then re-growing. Sampling of the deposit just after it had formed also showed that the gel contained a total wax with a concentration approximately six times the wax concentration in the oil, signifying that enrichment of precipitated wax near the vicinity of the cold finger occurred first before a stable gel was able to form. Details and discussion of this experiment are laid out in Appendix D of the Supplementary Information.

A more in-depth study on dilute and multicomponent waxy oils must be carried out to fully understand the significance and impact of C_{pi} on deposition and to identify if the cases with higher C_{pi} values presented in Appendix B are realistic. Such a study could include varying the initial concentration of wax in the oil and the stirring rate.

FIGURE 10 Measured mass transfer coefficient, k_c as a function of stirring rate [Color figure can be viewed at wileyonlinelibrary.com]
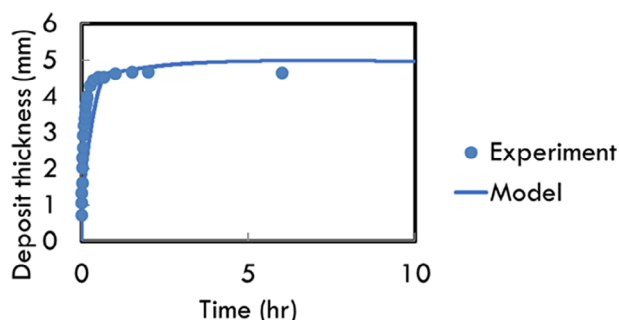
FIGURE 11 Deposit thickness versus time for the lowest stirring rate, 112 rpm [Color figure can be viewed at wileyonlinelibrary.com]

FIGURE 13 Deposit thickness versus time for the highest stirring rate, 417 rpm. The inset shows the deposit thickness during the first half hour [Color figure can be viewed at wileyonlinelibrary.com]

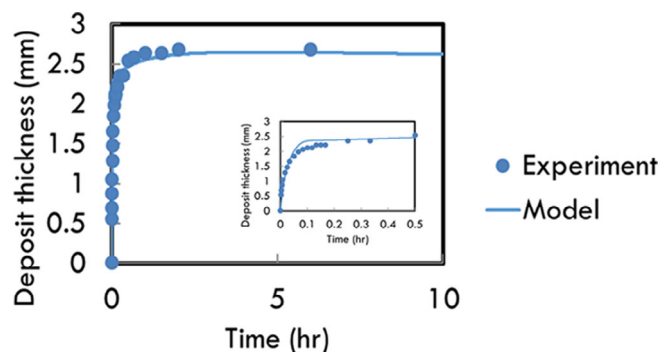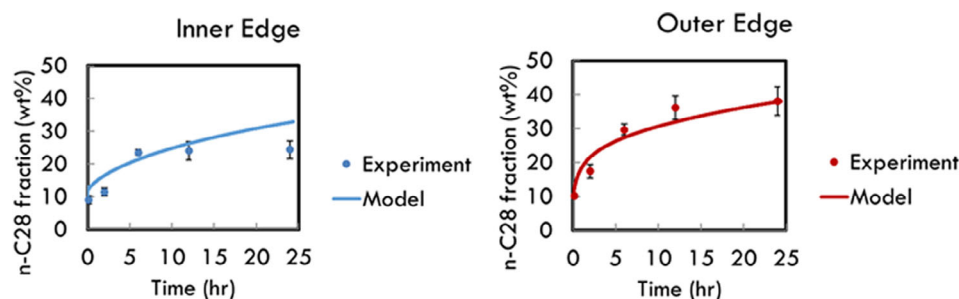FIGURE 12 Inner and outer deposit compositions for the lowest stirring rate, 112 rpm. To obtain the plotted predictions at the inner and outer edge, the predicted wax composition profiles, including both precipitated and dissolved wax, were integrated over the inner and outer 2 mm of the deposit (when thickness is greater than 4 mm) or the inner and outer halves of the deposit (when thickness is less than 4 mm) [Color figure can be viewed at wileyonlinelibrary.com]

FIGURE 14 Inner and outer deposit compositions for the highest stirring rate, 417 rpm. To obtain the plotted predictions at the inner and outer edge, the predicted wax composition profiles, including both precipitated and dissolved wax, were integrated over the inner and outer halves of the deposit [Color figure can be viewed at wileyonlinelibrary.com]

5 | CONCLUSIONS

A new transport model has been developed that predicts the formation of paraffin wax deposits and their aging from wax-containing oils. The behavior of the model was compared with results measured in a cold-finger experiment. The model includes transient energy and mass balances that must be solved simultaneously while allowing for the possible effects of yield stress on the deposition through a critical solid wax concentration at the deposit-fluid interface, C_{pi}. This new parameter is the precipitated wax concentration needed to withstand the shear stress imposed by the flow at the interface and reflects the dependence of the deposit yield stress on precipitate concentration and the fluid shear stress at the interface. While most our studies in a cold finger apparatus with a single dissolved wax component at 10% by weight show no indication that C_{pi} is significantly different from zero, we did find indications of its importance when wax content in the oil is low, around 1%. In addition, we expect its influence to be much more significant for multi-component waxes for which precipitation occurs more gradually with changing temperature than for a single-component wax. Future work will be needed to explore this possibility. We also allow the phase change from dissolved to precipitated wax to have a finite rate following a first-order reversible reaction rate law, but find our experimental results are explained well using an asymptotically high rate, implying instantaneous equilibrium can be assumed between precipitated and dissolved wax.

The most influential parameters in our experiments, namely the heat and mass transfer coefficients, are measured in the cold-finger apparatus at different stirring speeds, and the measured values are used in successful predictions of experimental results. Because of the reversible phase change, the model can predict the redissolution of precipitated waxes that may occur during deposit aging, which has been observed experimentally. In addition to obtaining the time evolution of the deposit thickness, this model also correctly predicts: (a) the spatial and temporal evolution of temperature and wax concentration in the deposit, and (b) the temporal evolution of temperature and wax concentration in the fluid, which are assumed to be spatially uniform. While the equations were developed to predict wax deposition onto a cold finger, similar equations can be adapted to other geometries as well, such as pipe flow.

NOTATION

t	time (s or hr)
ρ	density of the oil and deposit (kg/m^3)
ΔH	specific latent heat of wax crystallization (J/kg)
δ	deposit thickness (m or mm)
k	thermal conductivity of deposit (W/m/°C)
$\hat{c}_p$	specific heat capacity of oil and deposit (J/kg/°C)
α	thermal diffusivity of oil and deposit (m^2/s)
T	temperature at a radial location in the deposit (°C)
T_{jac}	set point temperature of heating water (°C)
$T_{\mathrm{jac,in}}$	temperature of water entering jacket (°C)
$T_{\mathrm{jac,out}}$	temperature of water leaving jacket (°C)
T_{cf}	set point temperature of cooling water (°C)
$T_{\mathrm{cw,in}}$	temperature of cooling water entering cold finger (°C)
$T_{\mathrm{cw,outer}}$	temperature of cooling water leaving cold finger (°C)
$T_{\mathrm{cf,out}}$	temperature on the cold finger outer surface(°C)
T_b	temperature of the oil (°C)
T_i	temperature at the deposit-oil interface (°C)
r	radial coordinate (m)
$r_{\mathrm{cf,in}}$	inner radius of stainless steel cold finger (m)
$r_{\mathrm{cf,out}}$	outer radius of stainless steel cold finger (m)
r_{jac}	inner radius of jacketed beaker (m)
L_l	height of liquid in the jacketed beaker (m)
L_{cf}	height of gel deposit along the cold finger axis (m)
U_{jac}	overall heat transfer coefficient for the heat transfer between the jacket and the solution (W/m^2/°C)
U_i	overall heat transfer coefficient for the heat transfer between the solution and the coolant inside the cold finger (W/m^2/°C)
h_{cf}	heat transfer coefficient for the heat transfer between the inner wall of the cold finger and the coolant (W/m^2/°C)
h_i	heat transfer coefficient for the heat transfer between the oil and the deposit (W/m^2/°C)

$\hat{h}_i$	normalized heat transfer coefficient for the heat transfer between the oil and the deposit (m/s)
A_{jac}	jacketed beaker surface area (m^2)
A_i	deposit-oil interfacial area (m^2)
m_{liq}	mass of oil in the reservoir (kg)
V_{liquid}	volume of oil in the reservoir (m^3)
$m_{total\,C28}$	total mass of n-C28 (kg)
C_s	soluble (i.e., dispersed) n-C28 concentration (kg/m^3)
$C_{s,eq}$	soluble wax concentration at the solubility limit (kg/m^3)
C_p	precipitated wax concentration in the deposit (kg/m^3)
C_{sb}	soluble wax concentration in the bulk oil (kg/m^3)
C_{pb}	precipitated wax concentration in the bulk oil (kg/m^3)
k_r	precipitation rate constant (s^{-1})
$D_{w/o}$	soluble wax diffusivity in precipitate-free oil based on the Hayduk-Minhas equation (m^2/s)
D_{eff}	effective soluble wax diffusivity in the deposit (m^2/s)
μ	viscosity of precipitated wax-free oil (mPa s)
V_A	molar volume of wax molecule (cm^3/mol)
K_α	dimensionless wax crystal aspect ratio

ORCID

Luqman Hakim Ahmad Mahir https://orcid.org/0000-0002-8117-4023

REFERENCES

1. Singh P, Venkatesan R, Fogler HS, Nagarajan N. Formation and aging of incipient thin film wax-oil gels. *AIChE J*. 2000;46(5):1059-1074. https://doi.org/10.1002/aic.690460517.
2. Huang Z, Lee HS, Senra M, Scott FH. A fundamental model of wax deposition in subsea oil pipelines. *AIChE J*. 2011;57(11):2955-2964. https://doi.org/10.1002/aic.12517.
3. Singh A, Lee HS, Singh P, Sarica C. Flow assurance: validation of wax deposition models using field data from a subsea pipeline. Paper presented at: Offshore Technology Conference; 2011. doi:https://doi.org/10.4043/21641-ms
4. Singh P, Venkatesan R, Scott Fogler H, Nagarajan NR. Morphological evolution of thick wax deposits during aging. *AIChE J*. 2001;47(1):6-18. https://doi.org/10.1002/aic.690470103.
5. Singh P, Youyen A, Fogler HS. Existence of a critical carbon number in the aging of a wax-oil gel. *AIChE J*. 2001;47(9):2111-2124. https://doi.org/10.1002/aic.690470921.
6. Tiwary R, Mehrotra AK. Deposition from wax-solvent mixtures under turbulent flow: effects of shear rate and time on deposit properties. *Energy Fuel*. 2009;23(3):1299-1310. https://doi.org/10.1021/ef800591p.
7. Haj-Shafiei S, Serafini D, Mehrotra AK. A steady-state heat-transfer model for solids deposition from waxy mixtures in a pipeline. *Fuel*. 2014;137(1):346-359. https://doi.org/10.1016/j.fuel.2014.07.098.
8. Bhat NV, Mehrotra AK. Modeling of deposit formation from "waxy" mixtures via moving boundary formulation: radial heat transfer under static and laminar flow conditions. *Ind Eng Chem Res*. 2005;44(17):6948-6962. https://doi.org/10.1021/ie050149p.
9. Kasumu AS, Mehrotra AK. Solids deposition from wax-solvent-water "waxy" mixtures using a cold finger apparatus. *Energy Fuel*. 2015;29(2):501-511. https://doi.org/10.1021/ef501835b.
10. Arumugam S, Kasumu AS, Mehrotra AK. Modeling of solids deposition from "waxy" mixtures in "hot flow" and "cold flow" regimes in a pipeline operating under turbulent flow. *Energy Fuel*. 2013;27:6477-6490. https://doi.org/10.1021/ef401315m.
11. Bidmus H, Mehrotra AK. Measurement of the liquid-deposit interface temperature during solids deposition from wax-solvent mixtures under static cooling conditions. *Energy Fuel*. 2008;22(2):1174-1182. https://doi.org/10.1021/ef700588y.
12. Bidmus HO, Mehrotra AK. Solids deposition during "cold flow" of wax-solvent mixtures in a flow-loop apparatus with heat transfer. *Energy Fuel*. 2009;23(6):3184-3194. https://doi.org/10.1021/ef900224r.
13. Arumugam S, Kasumu AS, Mehrotra AK. Modeling the static cooling of wax-solvent mixtures in a cylindrical vessel. Paper presented at: Proceedings of the Biennial International Pipeline Conference, IPC; 2012. doi:https://doi.org/10.1115/IPC2012-90691
14. Bidmus H, Mehrotra AK. Measurement of the liquid-deposit interface temperature during solids deposition from wax-solvent mixtures under sheared cooling. *Energy Fuel*. 2008;22(6):4039-4048. https://doi.org/10.1021/ef800542a.
15. Mahir LHA, Vilas Bôas Fávero C, Ketjuntiwa T, Fogler HS, Larson RG. Mechanism of wax deposition on cold surfaces: gelation and deposit aging. *Energy Fuel*. 2019;33(5):3776-3786. https://doi.org/10.1021/acs.energyfuels.8b03139.
16. Crank J. *Free and Moving Boundary Problems*. Oxford: Clarendon Press; 1984.
17. Hayduk W, Minhas BS. Correlations for prediction of molecular diffusivities in liquids. *Can J Chem Eng*. 1982;60(2):295-299. https://doi.org/10.1002/cjce.5450600213.
18. Cussler EL, Hughes SE, Ward WJ, Aris R. Barrier membranes. *J Membr Sci*. 1988;38(2):161-174. https://doi.org/10.1016/S0376-7388(00)80877-7.
19. Crank J, Nicolson P. A practical method for numerical evaluation of solutions of partial differential equations of the heat-conduction type. *Math Proc Cambridge Philos Soc*. 1947;43:50-67. https://doi.org/10.1017/S0305004100023197.
20. Rice Richard G., Do Duong D. *Applied Mathematics and Modeling for Chemical Engineers*. 2nd ed. Hoboken, New Jersey: Wiley; 2012.